PNAS RESEARCH ARTICLE | ENGINEERING

Strain learning in protein-based mechanical metamaterials

Naroa Sadaba[a,b,1], Eva Sanchez-Rexach[a,b,1], Curt Waltmann[c], Shayna L. Hilburg[d], Lilo D. Pozzo[d], Monica Olvera de la Cruz[c,2], Haritz Sardon[b,2], Lucas R. Meza[e,2], and Alshakim Nelson[a,2]

Affiliations are included on p. 6.

Edited by Joanna Aizenberg, Harvard University, Allston, MA; received April 23, 2024; accepted September 4, 2024

Mechanical deformation of polymer networks causes molecular-level motion and bond scission that ultimately lead to material failure. Mitigating this strain-induced loss in mechanical integrity is a significant challenge, especially in the development of active and shape-memory materials. We report the additive manufacturing of mechanical metamaterials made with a protein-based polymer that undergo a unique stiffening and strengthening behavior after shape recovery cycles. We utilize a bovine serum albumin-based polymer and show that cyclic tension and recovery experiments on the neat resin lead to a ~60% increase in the strength and stiffness of the material. This is attributed to the release of stored length in the protein mechanophores during plastic deformation that is preserved after the recovery cycle, thereby leading to a "strain learning" behavior. We perform compression experiments on three-dimensionally printed lattice metamaterials made from this protein-based polymer and find that, in certain lattices, the strain learning effect is not only preserved but amplified, causing up to a 2.5× increase in the stiffness of the recovered metamaterial. These protein–polymer strain learning metamaterials offer a unique platform for materials that can autonomously remodel after being deformed, mimicking the remodeling processes that occur in natural materials.

strain learning | protein | mechanical metamaterial | additive manufacturing | shape memory

Significance

We established a strain learning mechanical metamaterial that can not only recover after plastic deformation but also become stronger and stiffer in response to the applied loads. We demonstrate that shape-memory protein–polymer networks can unravel to release their stored length and, after recovery, will reconfigure to accommodate higher loads. These materials are incorporated into lattice frameworks using additive manufacturing which are then shown to become up to 2.5× stiffer after being crushed to 80% strain and recovered. This strain learning behavior enables the creation of metamaterials that are "teachable" and can autonomously remodel in response to applied loads, similar to the processes that occur in natural materials.

Biological materials such as bone and spider silk undergo stress-induced remodeling processes that enhance their mechanical properties. Bone can form stiffness gradients in response to force mechanotransduction (1–5) and unspun spider silk proteins are under constant shear stress during the fiber-forming process to enhance the strength of the filaments (6–11). Engineered materials that can mimic the stress-responsive features of these natural systems could enable autonomous materials that strengthen in response to mechanical cues from the environment for applications in the aerospace and medical fields (12). However, traditional synthetic thermosets are limited in their ability to adapt to mechanical forces, and in many cases, the materials become weaker or more brittle after mechanical deformation (10). Bonds cleavable via homolytic scission or dynamic covalent reactions can provide mechanisms for stress relaxation, but these materials do not necessarily afford a thermoset with improved mechanical strength (13). Alternatively, reactive strand expansion also provides a molecular-scale mechanism for dissipating stress within a network by utilizing polymers that can release their "stored length" (14–19). All of these approaches are effective for mitigating stress and damage within a cross-linked polymer network, but to the best of our knowledge, have not led to stress-induced enhancement of mechanical properties that is analogous to biological systems.

Protein-based synthetic materials can replicate some of the features of natural systems, but the processability of proteins into functional materials with defined 3D form factors can be challenging. Silk protein can afford materials with excellent mechanical characteristics, however, its propensity to aggregate in solution can hamper its processability via additive manufacturing processes (20). Alternatively, bovine serum albumin (BSA) is a globular protein that is highly processible due to its compact globular shape and high degree of solubility. BSA has recently been developed into resins for vat photopolymerization to afford shape-morphing bioplastic constructs (21, 22). Resin formulations comprising BSA and poly(ethylene glycol) diacrylate (PEGDA) were used to fabricate protein–polymer networks with defined 3D geometries. In these networks, BSA functioned as mechanophores, but rather than triggering a chemical reaction in response to mechanical force as traditional mechanophores do, they released their stored length when subjected to mechanical deformation. Upon the application of a mechanical load, the unfolding of these globular proteins in the network conferred an energy dissipation mechanism that introduced plasticity into the material and a greater resistance to failure. Furthermore, the original object shape was then recovered via heat or hydration. With small strains, a strain stiffening effect was observed due to protein unfolding. However,

Author contributions: N.S., E.S-R., H.S., L.R.M., and A.N. conceived the project and designed the experiments; M.O.C., H.S., L.R.M., and A.N. supervised the project; C.W. and M.O.C. performed computational experiments; S.L.H. and L.D.P. collected and analyzed SAXS data; and N.S., L.R.M., and A.N. wrote the manuscript with contributions from all authors.

The authors declare no competing interest.

This article is a PNAS Direct Submission.

[1]N.S. and E.S.-R. contributed equally to this work.

[2]To whom correspondence may be addressed. Email: m-olvera@northwestern.edu, haritz.sardon@ehu.es, lmeza@uw.edu, or alshakim@uw.edu.

This article contains supporting information online at https://www.pnas.org/lookup/suppl/doi:10.1073/pnas.2407929121/-/DCSupplemental.

Published October 30, 2024.

the strain stiffening behavior was limited to small deformations up to 20% compressive strain, beyond which visible signs of mechanical damage to the material were observed. Thus, at large strains, the shape-recovered objects were always mechanically weaker than the original structure.

Mechanical metamaterials are architected constructs that exploit deformation, stress, and mechanical energy to engineer the constituent material properties. These materials rely on geometric designs to distribute mechanical loads, e.g., across lattice frameworks, to improve their deformability, recoverability, and stiffness relative to the constituent properties of the monolithic material (23, 24). Herein, we show that the integration of protein mechanophores that can release their stored length into 3D printed lattice geometries can afford mechanical metamaterials that become stiffer via a strain learning mechanism (Fig. 1). Thus, these metamaterials are designed across the molecular and macroscales to enable a hierarchical response to mechanical force.

Results and Discussion

Strain Learning Behavior via BSA Unfolding. A typical thermoset becomes stiffer as the number of cross-linking junctions increases, but this enhancement also comes with a decrease in the extensibility of the material (i.e., a decrease in toughness) (25). However, uniaxial tensile experiments on dogbone samples with varying ratios of BSA/PEGDA showed an unusual behavior in these materials: As the concentration of BSA junctions in the network increased, so did the Young's modulus and the elongation at break (Fig. 2*A*). We analyzed how the presence of BSA junctions in a polymer network affected the bulk mechanical properties by 3D printing three different compositions of BSA/PEGDA resins with weight ratios of 25/75, 50/50, and 75/25. All BSA/PEGDA samples exhibited improved mechanical properties relative to the neat material network. The BSA/PEGDA 75/25 showed a clear yield point followed by a plateau region representing the plastic deformation of the material. Thus, these protein–polymer thermosets enhance their tensile toughness with increasing amounts of protein, which is attributed to the release of protein stored length.

The experimental results were supported with coarse-grained molecular dynamics simulations of the BSA/PEGDA networks comprising the same mass ratios of BSA to PEGDA. Given the huge computational resources of the all-atom model of BSA, we developed a simpler coarse-grained model (*SI Appendix*, Fig. S3). The Go-like model (26–28) allows for bond breaking and the uniaxial deformation of the material was considered at a constant volume and strain rate of 100% ns^{-1}. These simulations showed that the strain at the onset of material failure (the point where 20 bonds are broken) was 110, 124, and 147% for BSA/PEGDA compositions of 25/75, 50/50, and 75/25, respectively. The simulations correlate closely with the values from the uniaxial tensile experiments and confirmed that BSA content improves the mechanical properties of these networks. While BSA has approximately 30 surface lysines, it is difficult to quantify the degree of functionalization of the proteins in these resins. Interestingly, our simulations show that the onset of material failure is independent of the number of PEG chains bound to the surface of the protein (between 11 and 25).

Understanding the protein's behavior within the network, we devised a strain learning regimen for these materials. By examining the stress–strain curve of BSA/PEGDA 75/25, we opted to subject them to varying strains: one below the yield point (12.5%) and others above (25, 50, 75, and 100%). Leveraging the hydration-induced shape memory feature of these materials (21, 22), we applied the respective strain, restored their shape (99% recovery) via hydration and dehydration of the samples, and then reapplied stress until failure (Fig. 2*D*). When the load applied to the network is below the yield point of the material, the mechanical properties (elastic modulus, elongation-at-break, and yield point) remain unchanged after shape recovery. On the contrary, if the applied force exceeds the yield point and enters the plastic region, the properties are modified due to the unfolding of the protein. Regardless of the force applied, once the yield point is exceeded, the shape-recovered dogbones demonstrated an elastic modulus and yield strength nearly doubled in value. For example, when a strain of 25% was applied, a modulus of 309 ± 21 MPa and a yield strength of 22 ± 1.1 MPa was obtained. After shape recovery (by immersing the sample in water and then dehydrating under ambient conditions), the elastic modulus and yield strength increased to 492 ± 23 MPa and 35 ± 1.2 MPa, respectively, representing a ~60% increase in the properties. The enhanced mechanical properties are attributed to the reconfiguration of the unfolded BSA after shape recovery.

Small-angle X-ray scattering (SAXS) of the networks showed the nanoscale behavior within these protein–polymer networks upon compression and recovery (Fig. 2*F*). A feature corresponding to the length scale of BSA (at approximately Q = 0.115 $Å^{-1}$, corresponding

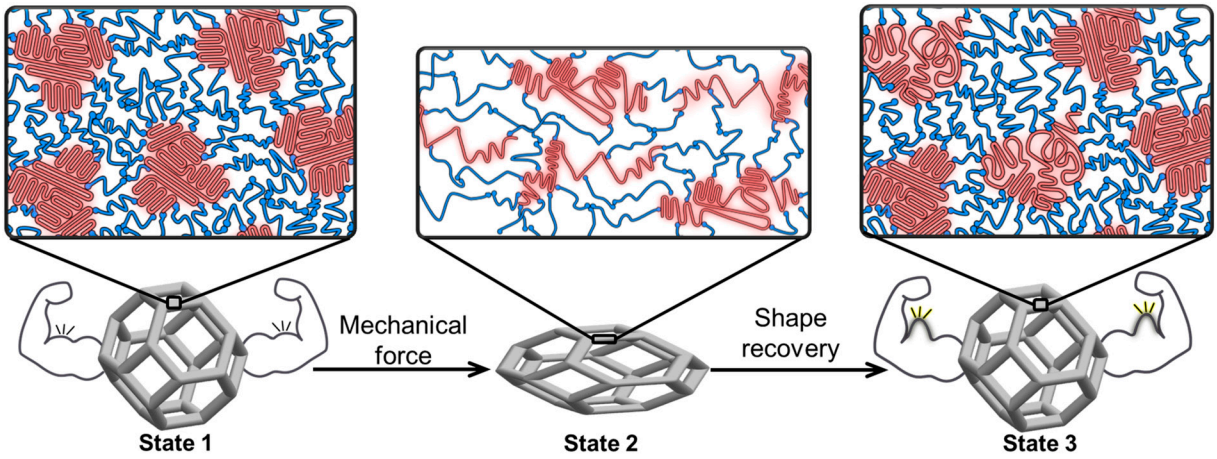

Fig. 1. Overview of the strain learning process, which utilizes 3D printed BSA/PEGDA networks that exhibit shape memory behavior. The strain learning behavior requires two steps. First, a mechanical force is applied to transform the shape of the object from state 1 to state 2. The plasticity of these materials is a consequence of the BSA junctions that release their stored length in the presence of a mechanical load. Then, the shape recovery process is performed to transform the object from state 2 to state 3. While the original shape is recovered, the proteins do not necessarily recover their native globular form, which leads to enhanced mechanical properties. The 3D printed lattice geometry (altered based on the computer-aided design) serves to minimize the mechanical damage by efficiently distributing stress across the entire structure.

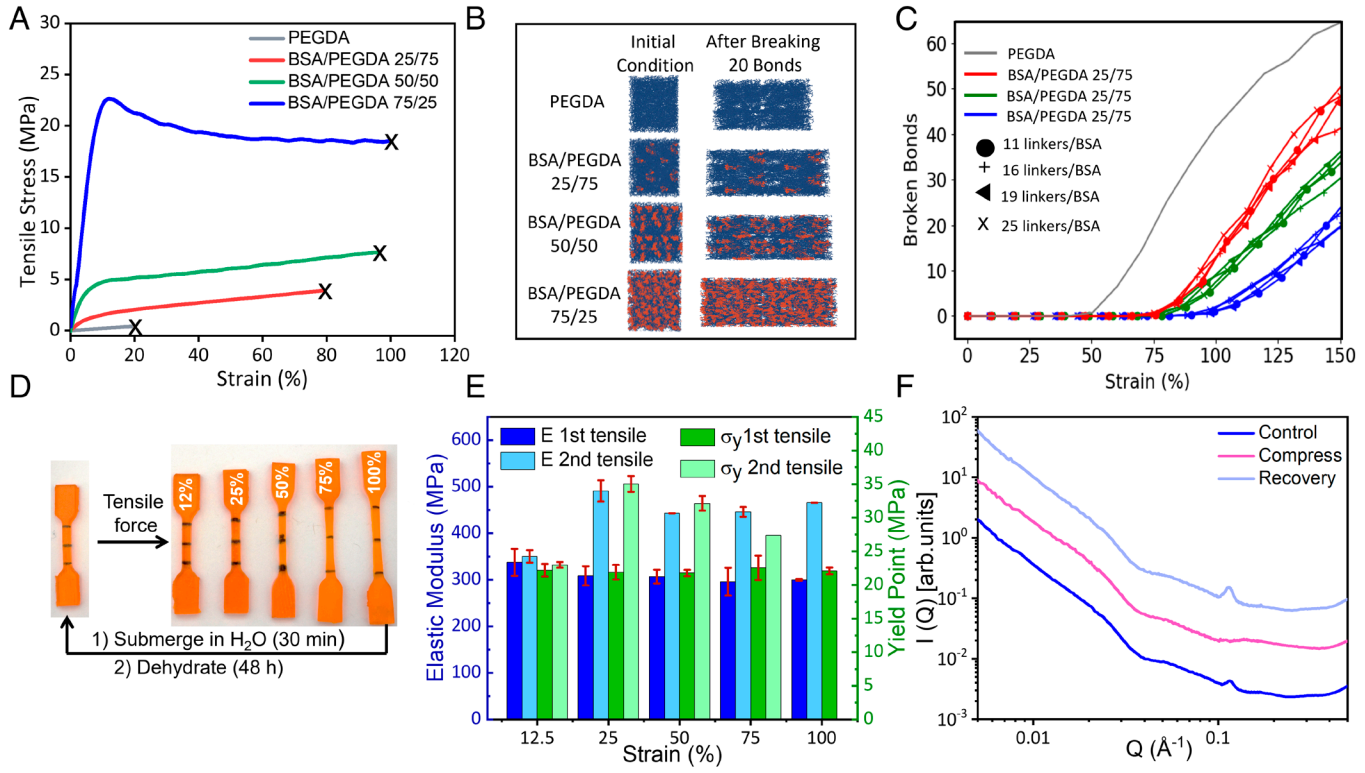

Fig. 2. Characterization of BSA/PEGDA networks before and after mechanical loading shows the release of the stored length in the protein junctions. (*A*) Uniaxial tensile experiments were performed on dogbone samples of PEGDA, BSA/PEGDA compositions of 25/75, 50/50, and 75/25. (*B* and *C*) Coarse-grained molecular dynamics simulations of the BSA/PEGDA networks with the same composition as the tensile specimens. The number of polymer chains per protein were varied in the simulations from 11 to 25, but this variation did not have a significant effect on the response of the proteins to applied strain. (*D* and *E*) Dogbone samples of BSA/PEGDA 75/25 were pulled to the different strains shown. The original dogbone length was recovered after submerging in H2O and dehydrating the sample, and then, the uniaxial tensile experiment was repeated. Samples with strains higher than 12% showed a higher modulus in the second cycle. (*F*) SAXS was performed on BSA/PEGDA 75/25 samples to compare the as-printed bioplastic (control), the compressed bioplastic, and the recovered bioplastic.

to 5.5 nm in real-space) in the initial sample is no longer seen after compression, exhibiting a reduction in molecular order upon deformation as schematically depicted in (Fig. 1, State 2). Interestingly, shape recovery (via hydration and subsequent dehydration) recovers this feature with even greater intensity than initially present (Fig. 1, State 3). The peak corresponding to 5.5 nm re-emerging after hydration recovery suggests that the BSA is refolding to a globular form that is comparable in size to its native state. The reduction and re-emergence of the feature are repeatable after an additional cycle of compression and hydration recovery (*SI Appendix*, Fig. S10*A*). In contrast, thermal shape recovery (via heating at 120 °C) does not recover this scattering peak, and instead, the scattering profile indicates disordered aggregates of denatured BSA molecules (*SI Appendix*, Fig. 10*B*). Thermal shape recovery at this temperature promotes denaturation and protein refolding does not occur. Therefore, the compression samples can only be cycled twice using thermal recovery before catastrophic sample failure occurs, while the samples recovered via hydration and drying could be cycled ten times.

The SAXS measurements indicated consistent structural recovery via hydration for both compression and tensile experiments (*SI Appendix*, Fig. S11). We additionally observed that tensile deformation of the sample caused the material to become oriented along the stretching axis. The degree of orientation, calculated with a tensor approach method (1 is perfectly aligned, 0 is fully isotropic) for a Q-range of 0.089 to 0.150 $Å^{-1}$ at sample-to-detector distance of 370 mm (29), depended upon the tensile strain. The first cycle of tensile stretching (75% strain) led to a degree of orientation of 0.170, and the second cycle (50% strain to break) led to a 0.123 degree of orientation. Interestingly, upon hydration recovery and drying of the sample, the network returned to a nearly isotropic state, showing at most 0.005 degree of orientation over the same Q-range after recovery from either deformation cycle and for the as-printed sample. These data further suggest protein unfolding during mechanical deformation (Fig. 1, State 2) and protein refolding during the shape recovery (back to Fig. 1, State 3).

Metamaterial Design for Energy Dissipation in Shape Memory Bioplastics. We fabricated lattice-based metamaterials that exhibit varying degrees of stress-induced stiffening depending on their architecture, thereby capitalizing on the strain hardening observed in the constituent material. We used three lattice architectures—octet-truss (OT), truncated octahedron (TO), and twisted truncated octahedron (TTO) (Fig. 3) and printed them using the BSA/PEGDA 75/25 mixture as it demonstrated the best mechanical performance. The lattices were each made with three different relative densities of ρ = 6, 9, and 12%. The OT lattice has been extensively studied in the literature, as has the TO lattice (also known as a Kelvin cell) (23, 30–32). The TTO lattice was initially developed as a tensegrity architecture capable of sustaining a prestress (33, 34), but it should be noted that this and other works on this architecture using additive manufacturing (35, 36) are not prestressed and thereby do not constitute a true tensegrity.

We performed uniaxial compression at quasistatic strain rates ($\dot{\varepsilon} = 10^{-3}$) on each of the lattices to characterize their strength, stiffness, and failure resistance after load-recovery cycles. It is well understood that the strength, stiffness, and energy dissipation depend strongly on the relative density, but these metrics do not capture the uniformity of the deformation in the lattice, which thereby affects the unfolding of the protein under an applied load. Fig. 3*A* shows how the

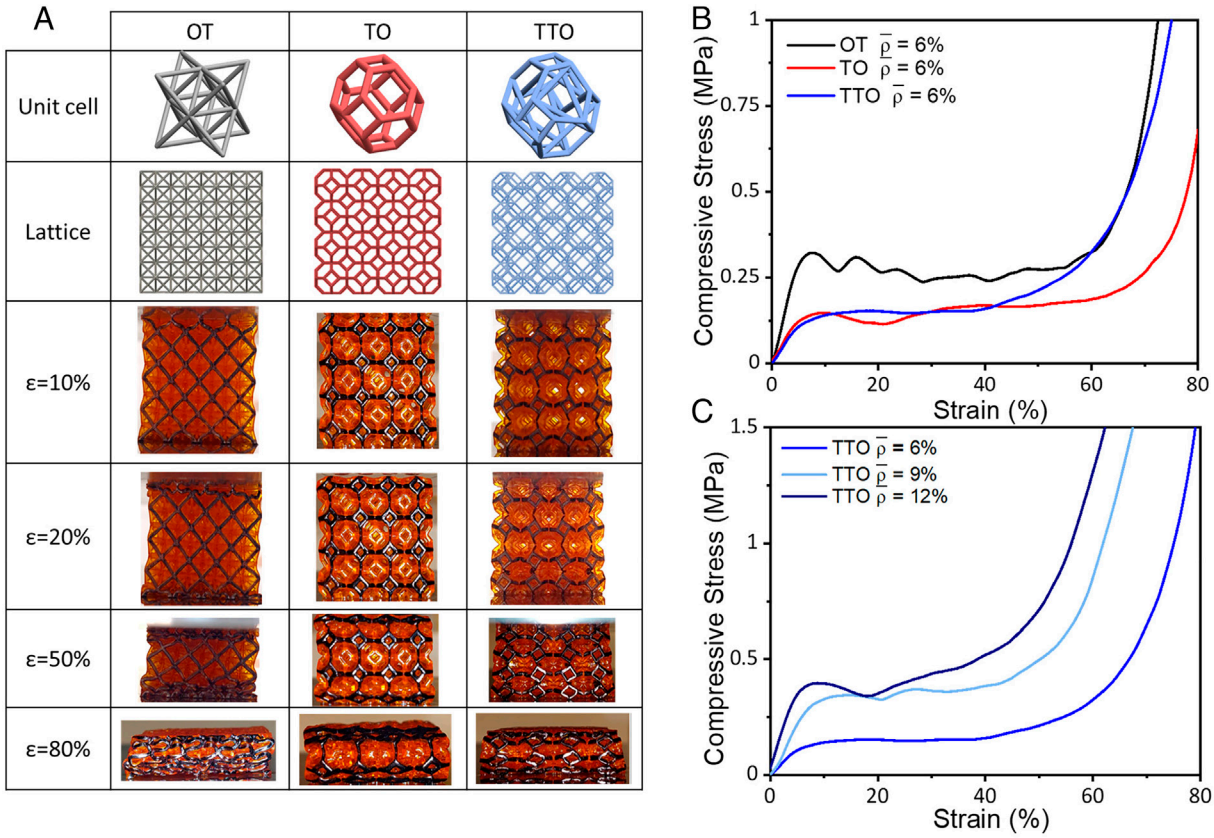

Fig. 3. Uniaxial compression experiments were performed on 3D printed OT, TO, and TTO lattices. (*A*) The images show that with increasing strain, the energy is dissipated differently based on the lattice design. The front face of the lattices in the optical images was colored with a black marker pen to provide contrast. (*B*) A plot that compares stress vs. strain curves for OT, TO, and TTO lattices with a density of 6%. (*C*) A plot that shows the stress vs. strain curves for TTO lattices with a density of 6, 9, and 12%.

energy is dissipated differently based on the lattice design. While the stress-strain responses of the lattices are similar—with a characteristic linear region, plateau region, and densification region—the OT and the TO lattices are not able to dissipate energy uniformly and experience a collapse in their top and bottom layers. This is because the beams of these lattices undergo buckling which causes a softening response and thereby a localization of deformation in a layer. This metamaterial localization causes high stress and corresponding damage at the material level in the collapsed beams. Reducing the density of these lattices reduces the amount of plastic deformation experienced by the slender beams, thereby promoting their resistance, but it does not mitigate the issue of localized failure. The TTO lattice uniquely does not experience any localization and has a uniform deformation throughout its structure even up to 80% strain. This behavior is observed regardless of relative density and only occurs with this lattice geometry.

The Young's modulus of lightweight materials is known to depend strongly on density. For lattices, there is an approximate scaling relationship of $E = CE_s\rho^m$, where C is a scaling coefficient, E_s is the constituent material modulus, and m is a scaling coefficient that is generally between 1 and 2 depending on the fraction of the lattice that carries load in tension/compression vs. in bending (37). For lattices with a relative density higher than ~5%, the nodes of the lattice significantly affect the load-carrying pathways such that any "bending" or "stretching" scaling assumptions are incorrect (31). The modulus-density scaling coefficients for the OT and TO lattices observed here are both m = 1.6 to 1.7, which matches well with previous observations for these lattice architectures in this density range whose properties are largely affected by nodal stress concentrations. Interestingly, the scaling coefficient for the TTO lattice is m = 0.75, but it should be noted that this is a misleading quantity because the mechanical efficiency (i.e., the C value) is low (*SI Appendix*, Fig. S12). These scaling coefficients are all also highly approximate due to the limited density range of specimens studied here.

To understand the differences in recoverability of the lattices at different densities, we must understand the role of the nodes as stress concentration points and of the strain in beams during bending. The sharp intersection between beams in a lattice naturally results in stress concentration. In high-density lattices, the proximity of the nodes amplifies their stress concentration effect, while low-density lattices carry load more optimally in tension or bending of their beams according to the rigidity of their topology (31). The smaller diameter beams in low-density lattices also experience a lower strain for the same amount of bending. This is directly reflected in the poor cyclic recoverability of all lattices at high relative density, which necessarily experience higher and less uniform local strains for the same global applied strain. The local strains will cause the constituent chains to unfold and harden, but if the strain exceeds the failure strain of the material, it will lead to damage. The differing levels of cyclic recoverability can thereby be understood in the context of a competition between local damage and global strain hardening of the constituent. Although our blends are capable of dissipating energy due to protein unfolding, they do not dissipate the energy uniformly throughout the material, and this can lead to failure.

As a comparative control experiment, we printed the TTO lattice using only PEGDA (*SI Appendix*, Fig. S13). As with BSA/PEGDA 75/25, an increase in modulus was observed with increasing lattice density. However, an important difference is that the PEGDA-only networks did not demonstrate an increase in stiffness when a second

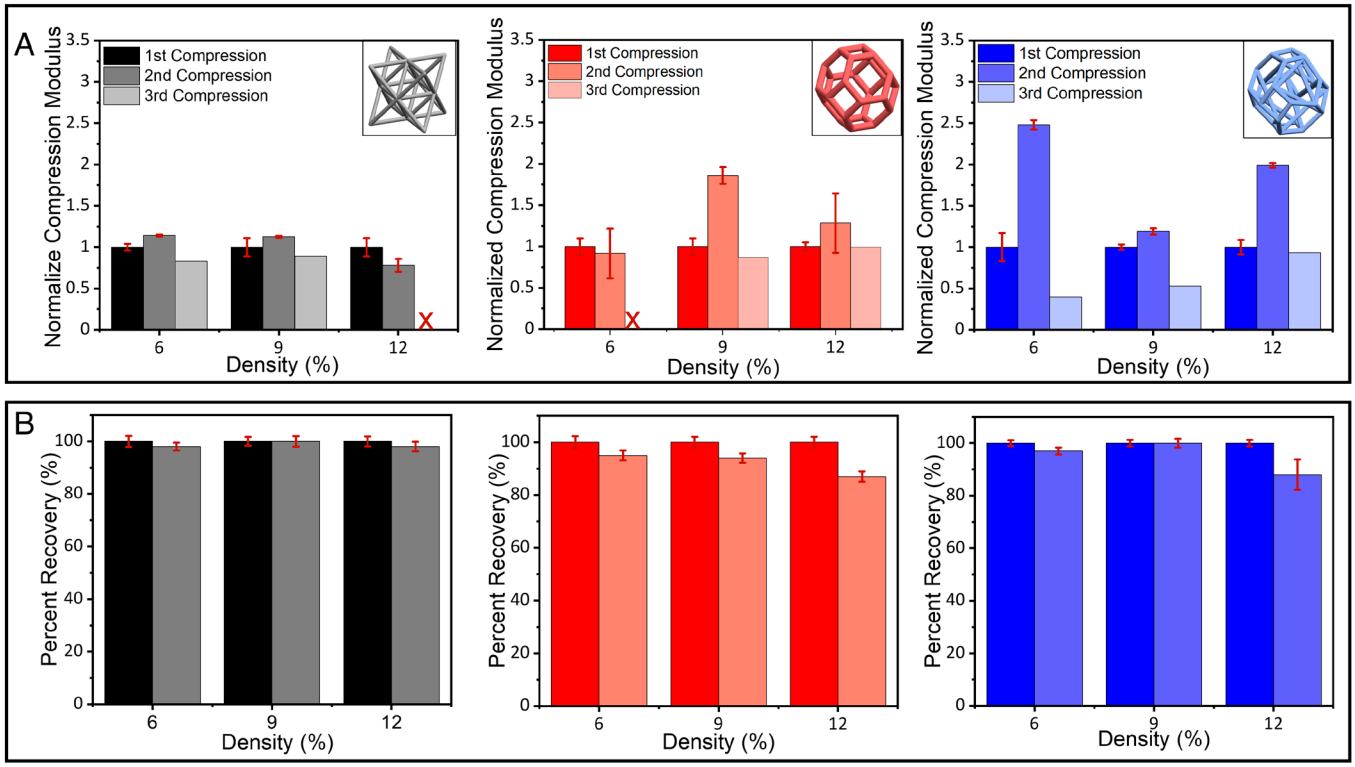

Fig. 4. Strain learning in multicycle compression test results for OT, TO, and TTO lattices. (*A*) Compressive moduli after 3 compression-recovery cycles. Each lattice, with a density of 6, 9, or 12% was compressed to 80% strain, recovered via hydration for 30 min, and dried for 48 h, before the next cycle of compression-recovery was performed. (*B*) Percent recovery for OT, TO, and TTO lattices with different densities.

cycle of compression was applied. In the case of density of ρ = 12% PEGDA-only sample, the structural integrity was lost during the first compression cycle.

Discussion

The 3D printed lattices showed mechanically induced stiffening after shape deformation and recovery. Strain learning experiments were performed to analyze the degree of shape recovery, the enhancement in modulus due to protein remodeling, and the number of cycles before lattice failure (Fig. 4). All the lattices were compressed to 80% strain and then recovered to 95% of their original size after a 30-min immersion in water followed by dehydration (Fig. 4*B*). Interestingly, the compression modulus increases from the first cycle to the second cycle as a consequence of the network structure remodeling that occurred as the BSA unfolded under mechanical load (Fig. 4*A*). Thus, the protein junctions present in the network release their stored length at the molecular scale to enable large deformations of the lattice at the macroscale. The presence of the permanent chemical cross-links in the network from the polymerized PEGDA provides the shape memory. It is possible that refolding of the proteins may also facilitate shape recovery during the hydration step since proteins have been observed to spontaneously refold in solution and in hydrogels (38–41). Our SAXS data (Fig. 2*F*) suggest that the proteins refold into globular structures with approximately 5.5 nm spacing after shape recovery. However, the enhanced mechanical stiffness that we observe (Fig. 4*B*) suggests that the proteins are not refolding back into their original state. Instead, the proteins are likely misfolded into globular conformations that ultimately strengthen the material. Of the three lattice designs tested, the TTO lattice with 6 and 12% showed the best performance with ~2.5-fold enhancement in the modulus between the first and second compression cycles (Fig. 4 and *SI Appendix*, Table S2). For the TTO lattice with density 9%, the modulus was similar between the first and second compression cycles. Across the three lattice designs, we observed the modulus to decrease during the third cycle, which is attributed to reduced ductility and the onset of damage in these materials once the original globular proteins were unfolded (*SI Appendix*, Fig. S14).

The synergy of protein mechanophores with 3D printed lattice architectures enables thermoset materials with unique mechanical responses to deformation. BSA is often a model protein employed in many contexts, and here, it served as a well-folded, single-chain globular protein that was incorporated into polymer networks during a vat photopolymerization process. The excellent solubility of this protein in aqueous solutions and the presence of surface lysines for functionalization contribute to its performance as a resin component for 3D printing.

An unexpected feature of these networks was the improvement in mechanical properties as the number of BSA junctions increased. Typically, as the number of junctions in a thermoset increases, there is an overall decrease in the toughness of the material. We observed that as the BSA concentration in the protein–polymer network increased, both the modulus and the strain at failure (and therefore, toughness) increased. Thus, these large globular proteins do not operate as traditional network junctions. We posit that other globular proteins with similar solubility and surface functionality should also demonstrate protein–polymer networks that exhibit unique mechanical responses based on protein primary, secondary, and tertiary structure. While naturally occurring proteins may fit this purpose, engineered proteins could hold the key to truly unlock the potential for these 3D printed protein–polymer networks.

Materials and Methods

Materials. Tris(2,2′-bipyridyl)-dichlororuthenium (II) hexahydrate [$Ru(bpy)_3Cl$] (99.95%), poly-(ethylene glycol) diacrylate (Mn = 700 g/mol), and sodium persulfate (SPS) were purchased from Sigma Aldrich. BSA was purchased from Nova Biologics. All the reagents were used as received.

BSA-Based Resin Preparation Protocol. The BSA-based resins were prepared according to the previously reported procedure22.

3D Printing. A Formlabs Form 2 printer was used to fabricate the 3D printed constructs, with 405 nm light and 250 mW intensity. 3D constructs were designed with Autodesk Fusion. The resin was poured into the resin tank, and the bioplastic constructs were then printed in Form 2's Open Mode with a layer height of 50 μm. Upon completion of the print, samples were removed from the build plate, rinsed in DI water to remove any uncured resin, and then air-dried for 48 h or 72 h. No post-curing process was needed.

Simulation Methods. In this section, we show the coarse-grained model of the protein BSA starting from atomistic simulations, which we compared to the coarse-grained model. We then show how we were able to incorporate the protein model into a gel model with breakable bonds that could be uniaxially deformed. In supplementary information, we show in detail how these simulations were carried out.

SAXS. Scattering experiments were measured on a Xenocs Xeuss 3.0 (Xenocs, Grenoble, France) instrument with a copper radiation source. Bioplastic samples initially 0.85 mm in thickness were measured as is, compressed, recovered by water, compressed–recovered–compressed, and compressed–recovered two full cycles by water. Also, we measured samples throughout the same two compression-recovery cycles, but recovered by heat rather than water (*SI Appendix*, Fig. S10). Three spots on each sample were tested and averaged. For each spot, scattering at sample-to-detector distances of 50, 370, 900, and 1,800 mm were collected for counting times of 90, 180, 270, and 450 s, respectively, in line eraser mode for full 2-D data collection. A set of data using tensile, rather than compressive, strain cycling was also collected (*SI Appendix*, Fig. S11). Tensile specimens originally 1 ± 0.01 mm in thickness were tested as is, strained to 75% strain, recovered by water, successively tensile strained for an additional 50% strain, and then recovered by water. One spot per sample at sample-to-detector distances of 50, 370, 900, and 1,800 mm were collected for counting times of 270, 540, 810, and 1,350 s, respectively. 2-D data were then reduced to 1-D and merged, subtracting background signal of the empty beam. Data processing was completed with XSACT software (Xenocs, Grenoble, France).

Mechanical Properties. Tensile tests were performed with a TA Electroforce TestBench uniaxial tension instrument at a speed of 5 mm/min until mechanical failure of the sample. The dogbones were 3D printed in the Form2 SLA printer, following the ISO 527-2 protocol. Compression samples for the lattice structures were 3D printed and dried, before being tested with an Instron 5585H 250 kN electromechanical test frame with a 50 kN load cell using a crosshead rate of 1.3 mm/min.

Data, Materials, and Software Availability. All study data are included in the article and/or *SI Appendix*.

ACKNOWLEDGMENTS. This research is financially supported by the Center for the Chemistry of Molecularly Optimized Networks, a NSF Center for Chemical Innovation (CHE-2116298). N.S. is grateful to the Universidad del Pais Vasco/Euskal herriko Univertsitatea (UPV/EHU) and the Margarita Salas fellowship for the requalification of the Spanish University system for 2021 to 2023, financed by the European Union (EU)-Next Generation. E.S.-R. H.S. acknowledges the financial support from el Ministerio de Ciencia e Innovación from TED2021-129852B-C22 funded by Ministerio de Ciencia Inovacion y Universidades/Agencia Estatal de Investigación (MCIU/AEI)/10.13039/501100011033 and by the European Union NextGenerationEU/Plan de Recuperación, Transformación y Resiliencia (PRTR) and the grant PID2022-138199NB-I00 funded by MCIU/AEI/10.13039/501100011033. We acknowledge the use of facilities and instrumentation (SAXS) supported by the U.S. NSF through the Major Research Instrumentation program (DMR-2116265) and by the University of Washington Molecular Engineering Materials Center, a Materials Research Science and Engineering Center (Grant No. DMR-2308979). All authors have given approval to the final version of the manuscript.

Author affiliations: [a]Department of Chemistry, University of Washington, Seattle, WA 98195; [b]POLYMAT and Department of Polymers and Advanced Materials: Physics, Chemistry and Technology, Faculty of Chemistry, Univesidad del Pais Vasco/Euskal Herriko Univertsitatea UPV/EHU, Donostia-San Sebastián 20018, Spain; [c]Department of Materials Science and Engineering, Northwestern University, Evanston, IL 60208; [d]Department of Chemical Engineering, University of Washington, Seattle, WA 98195; and [e]Department of Mechanical Engineering, University of Washington, Seattle, WA 98115

1. S. C. Cowin, Wolff's law of trabecular architecture at remodeling equilibrium. *J. Biomech. Eng.* **108**, 83–88 (1986).
2. M. J. Buehler, Nature designs tough collagen: Explaining the nanostructure of collagen fibrils. *Proc. Natl. Acad. Sci. U.S.A.* **103**, 12285–12290 (2006).
3. J. Wolff, *The Law of Bone Remodelling* (Springer Berlin, Heidelberg, 1986), 10.1007/978-3-642-71031-5.
4. C. Boyle, I. Y. Kim, Three-dimensional micro-level computational study of Wolff's law via trabecular bone remodeling in the human proximal femur using design space topology optimization. *J. Biomech.* **44**, 935–942 (2011).
5. K.-i. Tsubota *et al.*, Computer simulation of trabecular remodeling in human proximal femur using large-scale voxel FE models: Approach to understanding Wolff's law. *J. Biomech.* **42**, 1088–1094 (2009).
6. J. A. Wagner *et al.*, Stress-induced long-range ordering in spider silk. *Sci. Rep.* **7**, 15273 (2017), 10.1038/s41598-017-15384-8.
7. T. Giesa, M. Arslan, N. M. Pugno, M. J. Buehler, Nanoconfinement of spider silk fibrils begets superior strength, extensibility, and toughness. *Nano Lett.* **11**, 5038–5046 (2011).
8. S. Keten, Z. Xu, B. Ihle, M. J. Buehler, Nanoconfinement controls stiffness, strength and mechanical toughness of β-sheet crystals in silk. *Nat. Mater.* **9**, 359–367 (2010).
9. Z. Lv *et al.*, Mechanism of mechanical training-induced self-reinforced viscoelastic behavior of highly hydrated silk materials. *Biomacromolecules* **22**, 2189–2196 (2021), 10.1021/acs.biomac.1c00263.
10. B. Du, Y. Wu, S. Lu, Z. Yang, S. Huang, Spider-silk-inspired heterogeneous supramolecular network with strain-stiffening, high damping capacity, and supercontraction. *Adv. Funct. Mater.* **33**, 2306071 (2023), 10.1002/adfm.202306071.
11. Y. Zhang *et al.*, Natural silk spinning-inspired meso-assembly-processing engineering strategy for fabricating soft tissue-mimicking biomaterials. *Adv. Funct. Mater.* **32**, 2200267 (2022), 10.1002/adfm.202200267.
12. L. Montero De Espinosa, W. Meesorn, D. Moatsou, C. Weder, Bioinspired polymer systems with stimuli-responsive mechanical properties. *Chem. Rev.* **11**, 12851–12892 (2017), 10.1021/acs.chemrev.7b00168.
13. W. Denissen, J. M. Winne, F. E. Du Prez, Vitrimers: Permanent organic networks with glass-like fluidity. *Chem. Sci.* **7**, 30–38 (2016), 10.1039/c5sc02223a.
14. M. Abi Ghanem *et al.*, The role of polymer mechanochemistry in responsive materials and additive manufacturing. *Nat. Rev. Mater.* **6**, 84–98 (2020), 10.1038/s41578-020-00249-w.
15. D. A. Davis *et al.*, LETTERS Force-induced activation of covalent bonds in mechanoresponsive polymeric materials. *Nature* **459**, 68–72 (2009), 10.1038/nature07970.
16. M. Horst *et al.*, Understanding the mechanochemistry of ladder-type cyclobutane mechanophores by single molecule force spectroscopy. *J. Am. Chem. Soc.* **143**, 12328–12334 (2021).
17. Z. Wang *et al.*, Toughening hydrogels through force-triggered chemical reactions that lengthen polymer strands. *Science* **374**, 193–196 (2021).
18. E. M. Lloyd, J. R. Vakil, Y. Yao, N. R. Sottos, S. L. Craig, Covalent mechanochemistry and contemporary polymer network chemistry: A marriage in the making. *J. Am. Chem. Soc.***145**, 751–768 (2023), 10.1021/jacs.2c09623.
19. V. A. Bobrin *et al.*, Nano-to macro-scale control of 3D printed materials via polymerization induced microphase separation. *Nat. Commun.* **13**, 3577 (2022), 10.1038/s41467-022-31095-9.
20. S. H. Kim *et al.*, Precisely printable and biocompatible silk fibroin bioink for digital light processing 3D printing. *Nat. Commun.* **9**, 1620 (2018), 10.1038/s41467-018-03759-y.
21. E. Sanchez-Rexach *et al.*, 3D-printed bioplastics with shape-memory behavior based on native bovine serum albumin. *ACS Appl. Mater. Interfaces* **13**, 19193–19199 (2021).
22. S. Yu *et al.*, 4D Printed Protein-AuNR Nanocomposites with Photothermal Shape Recovery. *Adv. Funct. Mater.* **34**, 2311209 (2023), 10.1002/adfm.202311209.
23. X. Zheng *et al.*, Ultralight, ultrastiff mechanical metamaterials. *Science* **344**, 1369–1373 (2014).
24. A. Guell Izard *et al.*, Ultrahigh energy absorption multifunctional spinodal nanoarchitectures. *Small* **15**, 1903834 (2019), 10.1002/smll.201903834.
25. G. Nian *et al.*, Making highly elastic and tough hydrogels from doughs. *Adv. Mater.* **34**, 2206577 (2022).
26. T. G. W. Graham, R. B. Best, Force-induced change in protein unfolding mechanism: Discrete or continuous switch? *J. Phys. Chem. B* **115**, 1546–1561 (2011).
27. R. B. Best, E. Paci, G. Hummer, O. K. Dudko, Pulling direction as a reaction coordinate for the mechanical unfolding of single molecules. *J. Phys. Chem. B* **112**, 5968–5976 (2008), 10.1021/jp075955j.
28. D. De Sancho, R. B. Best, Reconciling intermediates in mechanical unfolding experiments with two-state protein folding in bulk. *J. Phys. Chem. Lett.* **7**, 3798–3803 (2016), 10.1021/acs.jpclett.6b01722.
29. D. K. Cinader, W. R. Burghardt, X-ray scattering studies of orientation in channel flows of a lyotropic liquid crystalline polymer. *Polymer (Guildf)* **40**, 4169–4180 (1999).
30. J. Bauer *et al.*, Nanolattices: An emerging class of mechanical metamaterials. *Adv. Mater.* **29**, 1701850 (2017), 10.1002/adma.201701850.
31. X. Zheng *et al.*, Ultralight, ultrastiff mechanical metamaterials. *Science* **344**, 1369–1373 (2014).
32. V. S. Deshpande, N. A. Fleck, M. F. Ashby, EEective properties of the octet-truss lattice material. *J. Mech. Phys. Solids* **49**, 1747–1769 (2001).
33. J. J. Rimoli, A re duce d-order model for the dynamic and post-buckling b ehavior of tensegrity structures. *Mech. Mater.* **116**, 146–157 (2017).
34. J. J. Rimoli, R. K. Pal, Mechanical response of 3-dimensional tensegrity lattices. *Compos. Part B: Eng.* **115**, 30–42 (2016), 10.1016/j.compositesb.2016.10.046.
35. K. Pajunen, P. Johanns, R. K. Pal, J. J. Rimoli, C. Daraio, Design and impact response of 3D-printable tensegrity-inspired structures-NC-ND license. *Mater. Des.* **182**, 107966 (2019).
36. J. Bauer *et al.*, Tensegrity metamaterials: Toward failure-resistant engineering systems through delocalized deformation. *Adv. Mater.***33**, e2005647 (2021), 10.1002/adma.202005647.
37. L. J. Gibson, M. F. Ashby, *Cellular Solids: Structure and Properties* (Cambridge University Press, ed. 2, 2014), 10.1017/CBO9781139878326.

38. L. R. S. Barbosa *et al.*, The importance of protein-protein interactions on the pH-induced conformational changes of bovine serum albumin: A small-angle X-ray scattering study. *Biophys. J.* **98**, 147–157 (2010).
39. M. Yahiya Khan, A. Salahuddin, Isolation, characterization and effect of acidic pH on the unfolding-refolding mechanism of serum albumin domains. *J. Biosci.* **15**, 361–376 (1990).
40. L. R. Khoury, I. Popa, Chemical unfolding of protein domains induces shape change in programmed protein hydrogels. *Nat. Commun.***10**, 5439 (2019), 10.1038/s41467-019-13312-0.
41. N. El Kadi *et al.*, Unfolding and refolding of bovine serum albumin at acid pH: Ultrasound and structural studies. *Biophys. J.* **91**, 3397–3404 (2006).